

Gapless Symmetry-Protected Topological States in Measurement-Only Circuits

Xue-Jia Yu,^{1,2,*} Sheng Yang,^{3,*} Shuo Liu,^{4,†} Hai-Qing Lin,³ and Shao-Kai Jian^{5,‡}

¹Department of Physics, Fuzhou University, Fuzhou 350116, Fujian, China

²Fujian Key Laboratory of Quantum Information and Quantum Optics,
College of Physics and Information Engineering,
Fuzhou University, Fuzhou, Fujian 350108, China

³Institute for Advanced Study in Physics and School of Physics, Zhejiang University, Hangzhou 310058, China

⁴Institute for Advanced Study, Tsinghua University, Beijing 100084, China

⁵Department of Physics and Engineering Physics,
Tulane University, New Orleans, Louisiana, 70118, USA

Measurement-only quantum circuits offer a versatile platform for realizing intriguing quantum phases of matter. However, gapless symmetry-protected topological (gSPT) states remain insufficiently explored in these settings. In this Letter, we generalize the notion of gSPT to the critical steady state by investigating measurement-only circuits. Using large-scale Clifford circuit simulations, we investigate the steady-state phase diagram across several families of measurement-only circuits that exhibit topological nontrivial edge states at criticality. In the Ising cluster circuits, we uncover a symmetry-enriched non-unitary critical point, termed symmetry-enriched percolation, characterized by both topologically nontrivial edge states and string operator. Additionally, we demonstrate the realization of a steady-state gSPT phase in a \mathbb{Z}_4 circuit model. This phase features topological edge modes and persists within steady-state critical phases under symmetry-preserving perturbations. Furthermore, we provide a unified theoretical framework by mapping the system to the Majorana loop model, offering deeper insights into the underlying mechanisms.

Introduction.—A modern frontier in quantum many-body physics involves investigating how exotic quantum states can emerge in non-equilibrium settings. These investigations are of fundamental interest and also related to quantum simulation experiments [1–4]. A prominent platform for investigating such phenomena is measurement-only quantum circuits incorporating non-commutative measurements [5, 6]. The competing measurements introduce a novel form of frustration, enabling the realization of quantum steady states characterized by distinct orders [7, 8] and entanglement patterns [9–23], as well as the transitions between them [24–57].

On a different front, recent advancements [58–90] have revealed that gapless quantum critical systems can support robust topological edge modes alongside critical bulk fluctuations [91–94]. This phenomenon, known as symmetry-enriched quantum criticality or gapless symmetry-protected topological (gSPT) phases [66–68], is characterized by topological edge modes [68], nontrivial conformal boundary conditions [63, 71], and a universal bulk-boundary correspondence encoded in the entanglement spectrum [72, 87].

However, realizing gSPT phases in solid-state materials remains a significant challenge, highlighting the potential of quantum simulators as a promising platform for achieving these exotic quantum critical states. This naturally raises the question: can the notion of gSPT be generalized to non-equilibrium settings, such as measurement-only circuits? If so, how can the underlying mechanisms behind these phenomena be analytically understood? To make progress in answering these questions, we investigate various families of measurement-only quantum circuits designed to gener-

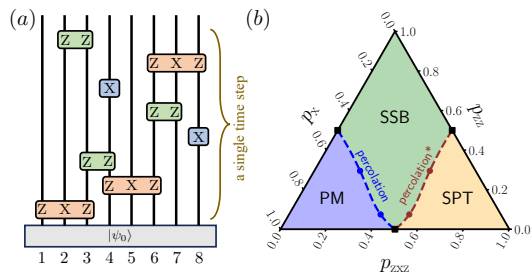


FIG. 1. (a) Circuit diagram of the Ising cluster circuit model with $L = 8$ qubits and 8 measurements (i.e., a single time step): blue, green, and orange rectangles represent the projective measurements X_i , $Z_i Z_{i+1}$, and $Z_{i-1} X_i Z_{i+1}$, respectively. (b) The steady-state phase diagram of the cluster circuit as a function of the probabilities p_x , p_{zz} , and p_{zxx} . The blue, green, and orange filled regions exhibit PM, SSB, and SPT orders, respectively. The red circles are critical points obtained by the data collapse of the generalized topological entanglement entropy [see Fig. 2(a) and Sec. II of the SM] and the red dashed line is a guide to the eye. Percolation* means the symmetry-enriched percolation universality. The blue circles and the corresponding dashed line are obtained by $p_x \leftrightarrow p_{zxx}$.

alize the notion of gSPT states to non-equilibrium settings. We firstly study the transition between different dynamical phases and reveal a new type of universality, termed *symmetry-enriched percolation*, featuring nontrivial boundary states. By generalizing and investigating the string operator with nontrivial symmetry flux, we find that the symmetry-enriched percolation cannot be connected to the conventional percolation without going through another fixed point, which in our case can be

as a double-copy of percolation. Beyond critical points, we further generalize the gSPT phases to non-equilibrium settings. Specifically, we study the steady state phase diagram of a \mathbb{Z}_4 circuit, in which a gSPT phase that features nontrivial edge states as well as critical fluctuations presents over a significant portion of the phase diagram. The transitions to non-topological phases, including percolation and Berezinskii–Kosterlitz–Thouless (BKT) transition, are also unbiasedly identified. Theoretically, the steady-state phase diagram can be understood by mapping the circuit model onto a Majorana loop model, providing a unified framework for investigating steady-state gSPT phases in 1+1D measurement-only circuits.

Setup.—We study two families of 1+1D measurement-only circuits, schematically illustrated in Fig. 1(a). The circuit architecture consists of measurements randomly applied with certain probabilities. These measurements are uniformly selected from possible locations along a one-dimensional qubit chain of length L under open boundary conditions (OBCs). The measurement protocol in this circuit is arranged as follows: A single-time step is defined as the application of L random measurement operations during the time evolution. Each measurement operator is randomly selected from a predefined set of operators according to a specified probability. Starting from an initial state $|\psi_0\rangle$, we evolve it over a large number of time steps (set to $5L$ unless otherwise specified) to reach a steady state. Subsequently, we compute the target physical quantities (defined in detail in Sec. I of the Supplementary Materials (SM)) and then average over different circuit realizations.

Symmetry-enriched percolation.—We consider a \mathbb{Z}_2 symmetric Ising cluster model defined by a set of measurement operators, $\{Z_{i-1}X_iZ_{i+1}, Z_iZ_{i+1}, X_i\}$, with corresponding probabilities p_{ZXZ} , p_{ZZ} and $p_X = 1 - p_{ZZ} - p_{ZXZ}$, respectively. The equilibrium counterpart of this model features a ground state phase diagram with three phases: ferromagnetic spontaneous-symmetry-breaking (SSB), trivial paramagnetic (PM), and symmetry-protected topological (SPT) phases. Importantly, while the SSB-PM and SSB-SPT transitions are both described by the Ising conformal field theory (CFT), the time-reversal symmetry acts differently on the disorder operator [68, 70], leading to distinct symmetry-enriched quantum critical points (QCPs).

In the measurement-only protocol described above, the ground-state phase diagram is replaced by a *steady-state* phase diagram, as shown in Fig. 1(b). It exhibits the non-equilibrium analogs of SSB (spin-glass order), trivial PM, and SPT order [7, 9, 10, 14]. The SPT (PM) phase emerges when p_{ZXZ} (p_X) dominates. These phases are separated by an SSB phase when p_{ZZ} is nonzero. We show that a nontrivial symmetry-enriched QCP emerges at the SSB-SPT transition at $p_{ZZ} = p_{ZXZ} = 1/2$, in stark contrast to the SSB-PM transition at $p_{ZZ} = p_X = 1/2$.

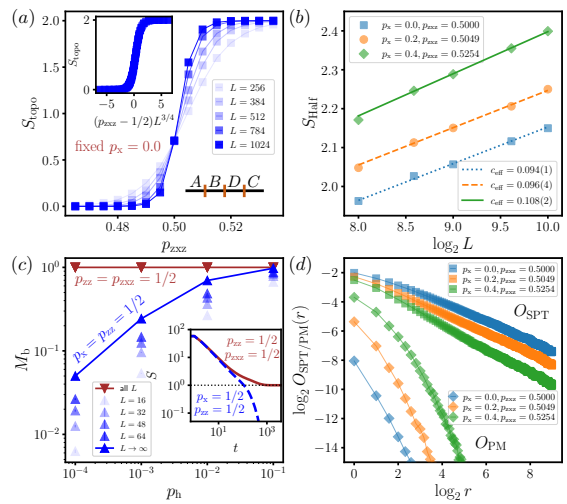


FIG. 2. (a) The generalized topological entanglement entropy S_{topo} versus p_{zxz} for different system sizes with fixed $p_x = 0$. $A|B|D|C$ represents the equal partition used in the definition of S_{topo} . The inset shows the data collapse of S_{topo} with $\nu = 4/3$ and $p_{\text{zxz},c} = 1/2$. (b) The half-chain entanglement entropy S_{Half} grows logarithmically as the system size increases at the critical points for the case of $p_x = 0.0, 0.2$, and 0.4 , respectively. The effective central charge c_{eff} are obtained from least-squares fittings. (c) The edge magnetization, $M_b \equiv (|\langle Z_1 \rangle| + |\langle Z_L \rangle|)/2$, in the presence of a small probability p_h of the boundary measurement $Z_{1/L}$ for the topologically trivial and nontrivial critical points, respectively. The inset shows the corresponding purification dynamics with an initial maximally mixed state for the same two critical points. (d) The string operators $O_{\text{SPT}}(r)$ (square markers) and $O_{\text{PM}}(r)$ (diamond markers) as a function of the lattice distance r at the critical points for the case of $p_x = 0.0, 0.2$, and 0.4 .

To this end, we consider topological entanglement entropy by partitioning the whole system into four subregions with equal size, $A|B|D|C$. S_{topo} is defined by $S_{\text{topo}} \equiv S_{AB} + S_{BC} - S_B - S_{ABC}$, where S_A denotes the entanglement entropy of a subsystem A . In Fig. 2(a), by examining S_{topo} , the critical point is located precisely at $p_{ZZ} = 1/2$, with a critical exponent $\nu = 4/3$. Furthermore, the half-chain entanglement entropy S_{Half} exhibits an effective central charge $c_{\text{eff}} = 0.094(1) \approx \frac{\sqrt{3}\ln 2}{4\pi}$ at the critical point, as shown in Fig. 2(b). These behaviors unambiguously demonstrate that the SSB-SPT transition belongs to the bond percolation universality class [95, 96]. While the SSB-PM transition also belongs to the percolation class [7, 33, 52], they are topologically distinct. To reveal the topological edge modes at steady-state criticality, we calculate the edge magnetization M_b as a function of the boundary field probability p_h across different system sizes under OBCs in Fig. 2(c). At the SSB-PM transition, the edge magnetization decreases with decreasing p_h (blue triangles), indicating the absence of edge modes. In contrast, at the SSB-

SPT transition, the edge magnetization remains finite (red solid line) as p_h approaches zero, providing direct evidence of topological edge modes at criticality. Moreover, in the inset, we show the full entanglement entropy under a purification dynamics, with the initial state being the maximally mixed state. The SSB-SPT (SSB-PM) transition shows a nonvanishing (vanishing) residue entropy $S(t) = 1$ ($S(t) = 0$) at late time $t \rightarrow \infty$, indicating the topological edge states.

The distinct topological properties suggest that these two QCPs cannot be adiabatically connected without going through another critical point. The phase diagram in Fig. 1(b) shows a generic path connecting the two QCPs, where the SSB-SPT (SSB-PM) transition is denoted respectively by the red (blue) dashed curves. The effective central charge is shown to be the same along these two transitions, as shown in Fig. 2(b), indicating that they both belong to the same percolation class; hence, it is crucial to show the distinction between the two QCPs along the path, as well as the emergence of another critical point. To this end, we use the following string operators [14, 68]:

$$O_{\text{PM}}(i, j) = \overline{|\langle X_i X_{i+1} \cdots X_{j-1} X_j \rangle|}, \quad (1)$$

$$O_{\text{SPT}}(i, j) = \overline{|\langle Z_{i-1} Y_i X_{i+1} \cdots X_{j-1} Y_j Z_{j+1} \rangle|}, \quad (2)$$

where $\langle \cdot \rangle$ denotes the expectation value taken in the steady state and $\overline{\cdot}$ denotes the average over steady states for different circuit realizations. Absolute value is also required to achieve a nonvanishing result [14]. Importantly, the SPT string operator $O_{\text{SPT}}(i, j)$ carries a nontrivial symmetry flux that is odd under time-reversal symmetry at the endpoints.

Figure 2(d) shows the SPT string operator dominates at the symmetry-enriched QCP along the SSB-SPT transition, whereas the PM string operator dominates at the SSB-PM transition (see SM Sec. II D). Since the two string operators carry distinct symmetry fluxes, they cannot be smoothly changed without another critical point. Indeed, the SPT-PM transition point at $p_X = p_{\text{ZXZ}} = 1/2$ is a different QCP with an effective central charge $c_{\text{eff}} = 2 \times \frac{\sqrt{3\ln 2}}{4\pi}$ that connects the symmetry-enriched SSB-SPT QCP and the SSB-PM QCP. Notice that the SPT-PM transition can be understood by two copies of percolation [9]. Therefore, our results reveal the emergence of *symmetry-enriched percolation* in the measurement-only circuit, making the first example of symmetry-enriched non-unitary CFT. Note that, in the Appendix, we use the Majorana loop model to provide a theoretical understanding of the symmetry-enriched QCP in this model.

gSPT phase in the steady state.—To extend the notion of topology to dynamical *critical phases*, we investigate the steady state of a \mathbb{Z}_4 -symmetric measurement-only circuit defined by a measurement operator set consisting of five different types of operators: The

first three types are inspired by the equilibrium intrinsic gSPT model [79, 84] (briefly reviewed in the SM Sec. III A), $\{\tau_{2i-1}^z \sigma_{2i}^x \tau_{2i+1}^z, \tau_{2i-1}^y \sigma_{2i}^x \tau_{2i+1}^y, \sigma_{2i}^z \tau_{2i+1}^x \sigma_{2i+2}^z\}$ with an equal probability p_t , and the last two types are competing measurements, $\{\tau_{2i-1}^x \tau_{2i+1}^x, \sigma_{2i}^x\}$ with corresponding probabilities, $\{p_\delta, p_h\}$. Note that $3p_t + p_\delta + p_h = 1$. Here, each pair of $(\tau_{2i-1}, \sigma_{2i})$ represents the i th unit cell, and the two species of spins per unit cell are represented by Pauli operators σ^α and τ^α . The operators possess a \mathbb{Z}_4 symmetry defined by $U = \prod_i \sigma_{2i}^x e^{i\frac{\pi}{4}(1 - \tau_{2i-1}^x)}$. The equilibrium counterpart exhibits an intrinsic gapless SPT state when the first three operators dominate. This phase is protected by an emergent anomaly of the \mathbb{Z}_4 symmetry.

Since the emergent anomaly is absent in the context of measurement-only circuits, where energy conservation does not apply, whether gSPT phases still exist in such settings is an outstanding question. We reveal an intriguing steady state phase diagram in Fig. 3 (a1), in which Phase I represents a gSPT phase with nontrivial edge states characterized by a nonvanishing residue entropy in the purification dynamics, nontrivial topological entanglement entropy, as well as critical correlation functions detailed below. Specially, Fig. 3(a2) shows the entanglement entropy under a purification dynamics: The red curve with a nontrivial residue $S = 1$ entropy indicates two degenerate states. Moreover, with nontrivial topological entanglement entropy at small but finite p_δ and p_h , Fig. 3(b1, b2) shows that the degeneracy in Phase I is originated from topological edge states. Finally, we can show that the steady state is also gapless by examining the string operator, $O_\tau(|i - j|) = |\langle \tau_{2i-1}^z (\prod_{k=i}^{j-1} \sigma_{2k}^x) \tau_{2j-1}^z \rangle|$, and the half-chain entanglement entropy. Figure 3(c1) shows a power law behavior of the string operator O_τ with an exponent $\Delta \approx 4/3$, and an effective central charge $c_{\text{eff}} \approx 2 \times \frac{\sqrt{3\ln 2}}{4\pi}$ in the inset. Later, we will see that the critical state is equivalent to two copies of percolation, which fully explains the observed c_{eff} .

Now let's discuss the transition to Phase II and III due to the competing measurement operators. The Phase III is an SSB state for both σ and τ degrees of freedom, induced by the perturbation $\tau_{2i-1}^x \tau_{2i+1}^x$. The residue entanglement entropy $S(t) = 2$ at late time in the purification dynamics is originated from the SSB for both σ and τ degrees of freedom, as shown by the dotted purple curve in Fig. 3(a2). The two-point functions of τ^x and σ^z both develop long-range correlation due to the SSB (detailed in the SM Sec. III C). The transition between the gSPT phase and the SSB phase belongs to the BKT universality class, as unveiled by a perfect data collapse of S_{topo} in Fig. 3(b1), which confirms a logarithmic-squared scaling form near the critical point [49]. Note that the topological entropy also decreases to zero due to the absence of topological edge state. On the other hand, the compet-

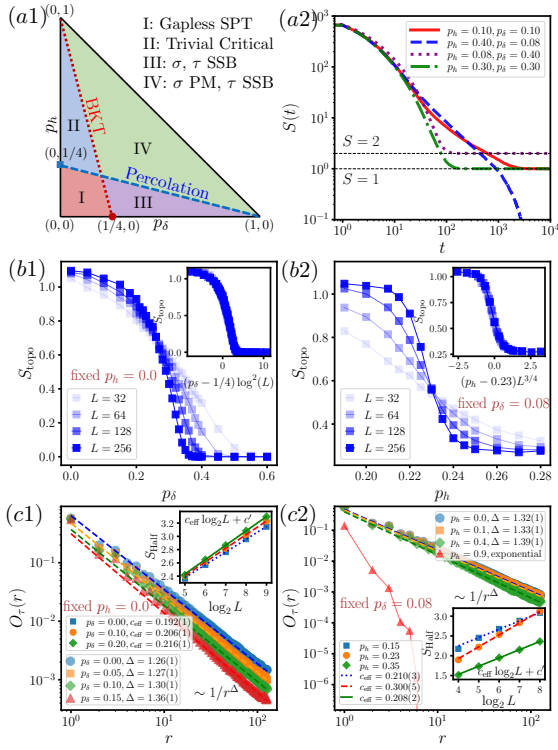


FIG. 3. (a1) Steady state phase diagram of the \mathbb{Z}_4 symmetric circuits. The BKT (percolation) transition line is $4p_\delta + p_h = 1$ ($4p_h + p_\delta = 1$) (see Sec. III B of the SM for additional numerical results). (a2) The evolution of the full system entropy, S , starting from a maximally mixed state for four representative points in different phases. S_{topo} as a function of p_δ at $p_h = 0$ (b1) and as a function of p_h at $p_\delta = 0.08$ (b2). The inset gives the data collapse of S_{topo} . (c1) The string operator $O_\tau(r)$ exhibits a power-law decay when $p_\delta \in [0, 0.25]$ for $p_h = 0$. Data within the interval $r \in (L/8, L/2)$ are used in the fittings and one end of the string operator was fixed at the boundary. The inset shows S_{Half} as a function of L . (c2) The string operator $O_\tau(r)$ exhibits a power-law dependence in the Phase I and Phase II, while an exponential decay in the Phase IV. The inset shows the logarithmic behavior of S_{Half} as a function of L for three representative points. The effective central charge c_{eff} is obtained from the least-squares fitting. The simulated system size is $L = 512$ in (a2) and $L = 256$ in (c1) and (c2).

ing measurement σ_{2i}^x leads to a transition to Phase II, which is a trivial critical phase without topological edge state. The string operator exhibits the same power law and the half-chain entanglement entropy also gives the same effective central charge, as shown in Fig. 3(c2) indicating the critical phase is of the same nature. However, the residue entropy, shown by the blue dashed curve in Fig. 3(a2), and the topological entropy in Fig. 3(b2) both vanish, demonstrating that Phase II is a non-topological gapless state. In Fig. 3(b2), we further reveal that the transition belongs to the percolation transition with the exponent $\nu = 4/3$. Lastly, Phase IV is an SSB phase for the τ degrees of freedom [97].

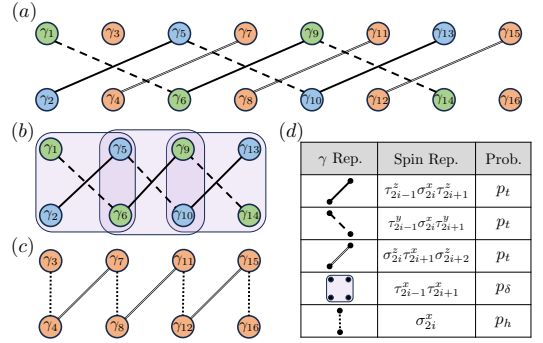


FIG. 4. Majorana representation of the \mathbb{Z}_4 symmetric circuit. (a) When $p_\delta = p_h = 0$, there are only three-site measurements $\{\tau_{2i-1}^z \sigma_{2i}^x \tau_{2i+1}^z, \tau_{2i-1}^y \sigma_{2i}^x \tau_{2i+1}^y, \sigma_{2i}^z \tau_{2i+1}^x \sigma_{2i+2}^z\}$; this model can be seen as two decoupled Majorana chains exhibited by (b) and (c). (b) The two-site perturbation $\tau_{2i-1}^x \tau_{2i+1}^x$ is added on the τ degrees of freedom, which is a four-Majorana operator. (c) The single-site perturbation σ_{2i}^x is added on the σ degrees of freedom. (d) gives the table of the associated projective measurements and their corresponding probabilities and Majorana representations.

Majorana loop models for measurement-only circuits.—We present a framework for the measurement-only circuit model based on the Majorana loop model to understand the numerical results. Here, we focus on the \mathbb{Z}_4 symmetric circuit. See the Appendix for more details.

First, consider the case without perturbation, i.e., $p_h = p_\delta = 0$. After performing the Jordan-Wigner transformation, the three-site measurements, $\tau_{2i-1}^z \sigma_{2i}^x \tau_{2i+1}^z$, $\tau_{2i-1}^y \sigma_{2i}^x \tau_{2i+1}^y$, and $\sigma_{2i}^z \tau_{2i+1}^x \sigma_{2i+2}^z$, are mapped to Majorana parity measurements, as shown in Fig. 4(a), on $(4i - 2, 4i + 1)$, $(4i - 3, 4i + 2)$ and $(4i, 4i + 3)$, respectively. In the Majorana representation, the whole system becomes two decoupled parts: τ -chain and σ -chain [see also Figs. 4(b) and 4(c) respectively]. It becomes evident that the edge modes are represented by the two dangling Majorana fermions in the σ -chain. In the absence of perturbation, the Majorana modes in the τ -chain can be further divided into two independent sets as shown in Fig. 4(b), which corresponds to two percolation models [49], whereas, the σ -chain is noncritical due to the dimerized pattern. Hence, the Majorana representation clearly unveils the gSPT steady state without perturbation.

Naively, the decoupled σ -chain resembles the Majorana representation of an Ising model, in which the two edge states account for the two-fold degeneracy from SSB. However, in terms of the spin operators in the \mathbb{Z}_4 circuit, the σ spin and the τ spin are strongly coupled. The gapless fluctuation in the τ -chain renders the correlation of σ spins gapless and disorders the seemingly SSB phase. This can be seen by noticing that the correlation of local spin operators $\sigma_{2i}^z \sigma_{2j}^z$ overlaps with the gapless Majorana in the τ -chain, preempting the SSB correlation. In-

stead, only the string operator $\sigma_{2i}^z (\prod_{k=i}^{j-1} \tau_{2k+1}^x) \sigma_{2j}^z$ purely overlaps with the dimerized Majorana, leading to a long-range correlation. In this sense, the topological edge state is protected by the gaplessness, and indeed, we will see in the following that once the gapless Majorana in the τ -chain is gapped out, the local spin operators $\sigma_{2i}^z, \sigma_{2j}^z$ acquire a long-range order, rendering the state non-topological.

The two-site measurement perturbation $\tau_{2i-1}^x \tau_{2i+1}^x$ corresponds to a non-Gaussian Majorana measurement as shown in Fig. 4(b) and induces couplings between the two percolation models (two τ -chains in the unperturbed circuit). When p_δ is small, these couplings are irrelevant [49, 98], the gSPT phase remains robust. When p_δ is large enough, the couplings between the two percolation chains become relevant and lead to a BKT transition to a noncritical state corresponding to the τ SSB phase in the spin picture. Moreover, the topological edge state from σ spins loses the protection and develops a long-range order. This is fully consistent with the σ and τ SSB in the Phase III.

Since the topological edge state is protected by the gapless fluctuations, relevant deformations that gap out the state will also render the state non-topological. For instance, unlike the equilibrium counterpart, the single-site operator τ_{2j+1}^x is a relevant perturbation at the fixed point with two copies of percolation [49]. We also investigate the effect of such a relevant perturbation, and find that indeed it leads to a transition from the gSPT phase to a σ SSB state (See SM Sec. III D for details). Of course, this perturbation can be forbidden by a \mathbb{Z}_2 symmetry, $\tau^x \rightarrow -\tau^x$.

Finally, the single-site measurement perturbation, σ_{2i}^x , simply leads to the coupling on $(4i-1, 4i)$, as indicated in Fig. 4(d), which is the other dimerization in Fig. 4(c). Since the σ chain and the τ chain are decoupled, the percolation transition at the equal strength of both dimerizations is consistent with the transition to the Phase II.

Concluding remarks.—To conclude, we uncover novel quantum phases and critical points in measurement-only circuits, including the first example of a symmetry-enriched non-unitary CFT and a steady-state gSPT phase with robust edge modes. By mapping these systems to the Majorana loop model, we also provide a unified framework for understanding these phenomena, highlighting measurement-only circuits as a powerful platform for exploring exotic quantum states and transitions.

Acknowledgement: We thank Ruochen Ma for helpful discussions. X.-J. Yu was supported by the National Natural Science Foundation of China (Grant No.12405034). This work is also supported by MOST 2022YFA1402701. S. Y. was supported by China Postdoctoral Science Foundation (Certificate Number: 2024M752760). The work of S.-K. J. is supported by a start-up grant and a COR Research Fellowship from Tulane University.

Appendix: More details on the Majorana loop

model and the cluster circuit model.—In the following, we present the details of the mapping from the measurement-only circuits to the Majorana loop models [49] and provide the theoretical understanding of the Ising cluster circuit model in Fig. 1.

To obtain the Majorana loop model, we first perform the Jordan-Wigner transformation to map the spin operators to the Majorana fermions,

$$\gamma_{2j-1} = \left(\prod_{k=1}^{j-1} X_k \right) Z_j, \quad \gamma_{2j} = \left(\prod_{k=1}^{j-1} X_k \right) Y_j, \quad (3)$$

where γ_{2j-1} and γ_{2j} are two Majorana fermions at site j and satisfy the anti-commutation relation $\{\gamma_m, \gamma_n\}_+ = 2\delta_{m,n}$. Subsequently, the projective measurements used in the measurement-only circuits can be mapped to the Majorana measurements as summarized in Fig. 4 for the \mathbb{Z}_4 circuit model. For the Ising cluster circuit model, the three types of projective measurements correspond to the following Majorana measurements,

$$X_j = i\gamma_{2j-1}\gamma_{2j}, \quad Z_j Z_{j+1} = i\gamma_{2j}\gamma_{2j+1}, \quad (4)$$

$$Z_{j-1} X_j Z_{j+1} = i\gamma_{2j-2}\gamma_{2j+1},$$

where $i\gamma_m\gamma_n$ is the Majorana parity measurement on flavors (m, n) . As a result, the projector for positive and negative parity is $\frac{1 \pm i\gamma_m\gamma_n}{2}$. As shown in Fig. 5(a), we use a single arc connecting γ_m and γ_n to represent the Majorana measurement $i\gamma_m\gamma_n$ regardless of the outcomes. We note that the measurements in the Ising cluster circuit model are all Gaussian Majorana measurements, while the $\tau_{2i-1}^x \tau_{2i+1}^x$ measurement in the \mathbb{Z}_4 circuit model is a non-Gaussian Majorana measurement. After establishing the transformation between the projective measurements in the spin basis and the Majorana measurements, we proceed to introduce the mapping from the measurement-only circuit to the Majorana loop model [49] via the following steps:

- 1). Firstly, the initial state can be represented by a specific pairing configuration of the Majorana fermions. For the initial product state $|\psi_{t=0}\rangle = \bigotimes_{i=1}^L |+\rangle_i$ considered in the work, where $|+\rangle_i$ is the eigenstate of X_i with +1 eigenvalue, it can be represented by Majorana fermions with a pairing configuration $\{(\gamma_1, \gamma_2), (\gamma_3, \gamma_4), \dots, (\gamma_{2L-1}, \gamma_{2L})\}$.
- 2). Subsequently, the Majorana parity measurements will rearrange the pairing configuration. For the Majorana fermions with pairing configuration $\{\dots, (\gamma_l, \gamma_m), (\gamma_n, \gamma_p), \dots\}$ at a discrete time step t , the parity measurement $i\gamma_m\gamma_n$ will break the original pairings (γ_l, γ_m) and (γ_n, γ_p) , and create new pairings (γ_l, γ_p) and (γ_m, γ_n) . Consequently, the pairing configuration at discrete time step $t+1$ is $\{\dots, (\gamma_l, \gamma_p), (\gamma_m, \gamma_n), \dots\}$. Therefore, the dynamics of the measurement-only circuits can be described by the dynamics of the Majorana pairing

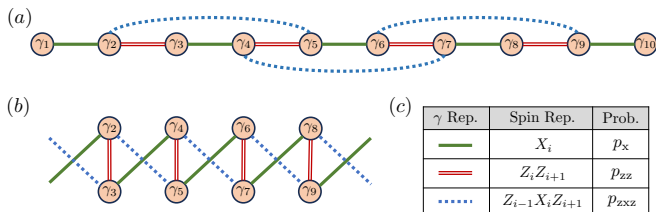


FIG. 5. Majorana representation of the cluster circuit model composed of X_i , $Z_i Z_{i+1}$, and $Z_{i-1} X_i Z_{i+1}$ measurements. (a) Each spin on site i is represented by two Majorana modes γ_{2i-1} and γ_{2i} . The green solid line, the red double solid line, and the blue dotted line represent the one-site X_i , the two-site $Z_i Z_{i+1}$, and the three-site $Z_{i-1} X_i Z_{i+1}$ measurements in the Majorana representation respectively. (b) A rearrangement of (a) preserving the linking structure under periodic boundary conditions. It is easy to see that there is a symmetry $p_x \leftrightarrow p_{zxx}$. (c) gives the table of the associated projective measurements and their corresponding probabilities and Majorana representations.

configurations along the time evolution, i.e., Majorana fermion worldlines.

Based on the points listed above, the instantaneous quantum state at discrete time t is determined by the corresponding Majorana pairing configuration (up to the sign of the parity), and thus the measurement-only circuits are mapped to the Majorana loop models.

Our observables have a direct correspondence in the Majorana loop model. Consider the von Neumann entanglement entropy S_R , where R is a contiguous system interval. In the Majorana loop model, it corresponds to the number of Majorana pairs, N_{pair} , in which one Majorana fermion is in the region R and the other is in the complement \bar{R} , and $S_R = N_{\text{pair}}/2$ [33, 52, 99]. Furthermore, the properties of the ensemble-averaged S_R are captured by the normalized arc length distribution $P(l)$ ($l = |m-n|$ is the pair length for the Majorana pair (γ_m, γ_n)), which is in one-to-one correspondence with the stabilizer length distribution in the clipped gauge [25, 100]. By tuning to the critical point, the ensemble of the Majorana loop model is described by the bond percolation conformal field theory (CFT) with critical exponent $\nu = 4/3$ and the length distribution $P(l)$ of the Majorana pairs obeys a universal form [51, 101] $l^2 P(l) \approx \frac{\sqrt{3}}{2\pi}$. This universal constant is then related to the prefactor c_{eff} in the logarithmic S_{Half} and $c_{\text{eff}} = \sqrt{3} \ln 2 / (4\pi)$ [49, 52].

The purification dynamics can also be understood from the perspective of the Majorana loop model. Unlike the case where the system starts from a product state with initial L Majorana pairings, as discussed earlier, there are no pairings at $t = 0$ when a maximally mixed state is chosen as the initial state in the purification dynamics. As time increases, Majorana fermion pairings are formed. The total entropy is $S(t) = \frac{1}{2} n_s(t)$, with $n_s(t)$ being the spanning number counting the unpaired Majorana

fermion modes. As detailed below, the distinct purification dynamics at SSB-PM and SSB-SPT transitions can be straightforwardly understood from the Majorana representations.

The Majorana loop model gives a straightforward understanding of the connection and distinction between the SSB-PM and SSB-SPT transitions. In the Majorana representation, the symmetry $p_x \leftrightarrow p_{zxx}$ used in Fig. 1 becomes transparent in Fig. 5(b). Consequently, in the absence of $Z_i Z_{i+1}$ measurement, the SPT-PM transition occurs at $p_x = p_{zxx} = 1/2$. Moreover, as shown in Fig. 5(b), it is obvious that the measurement-only circuit model corresponds to two decoupled Majorana chains and thus the critical point $p_x = p_{zxx} = 1/2$ is characterized by two copies of the critical percolation. However, it is also noted that the existence of the symmetry $p_x \leftrightarrow p_{zxx}$ does not mean that the two percolation lines related by this symmetry are completely equivalent. As shown in the main text and Section II in the Supplemental Materials, the SSB-SPT transition is different from the SSB-PM transition under open boundary conditions as revealed by the boundary magnetization, non-trivial residue entropy, and the dominated $O_{\text{SPT}}(r)$. The difference comes from the fact that the physical degree of freedom on site i is composed of the Majorana fermions, γ_{2i-1} and γ_{2i} , rather than γ_{2i-2} and γ_{2i+1} . Consequently, in the Majorana representation, there are two Majorana modes, γ_1 and γ_{2L} , unmeasured in the whole dynamics at the parameter point $p_{zz} = p_{zxx} = 1/2$ and $p_x = 0$ and induce the residue entropy $S = 1$ in the purification dynamics. In the setup with initial product states, these two Majorana modes are paired in the final state and a robust long-range entanglement is established in the system.

Further, the string operators in the Majorana representation ($m < n$ is assumed) read

$$\hat{O}_{\text{PM}} = \prod_{k=m}^n X_k \sim (i)^{n-m+1} \prod_{k=2m-1}^{2n} \gamma_k, \quad (5)$$

$$\begin{aligned} \hat{O}_{\text{SPT}} &= Z_{m-1} Y_m \left(\prod_{k=m+1}^{n-1} X_k \right) Y_n Z_{n+1} \\ &\sim (i)^{n-m+3} \gamma_{2m-2} \left(\prod_{k=2m}^{2n-1} \gamma_k \right) \gamma_{2n+1}. \quad (6) \end{aligned}$$

It is easier to consider SSB-PM transition with $p_{zxx} = 0$, while the case at the SSB-SPT transition can be understood similarly by the symmetry. Since the PM string operator \hat{O}_{PM} is a consecutive product of Majorana operators in an interval from m to n , it is nonvanishing only when Majorana fermions inside the interval are paired within themselves. Equivalently, a configuration with a pairing between a Majorana inside the interval and another Majorana outside is not allowed. With the mapping to the one-state Potts model [96, 102], this string operator corresponds to two boundary condition

changing (bcc) operators located at the end points of the interval. This bcc operator has a scaling dimension $\Delta_{\text{bcc}} = 1/3$, leading to a power law behavior with exponent $2\Delta_{\text{bcc}} = 2/3$ of the string operator \hat{O}_{PM} at the SSB-PM transition. On the contrary, the SPT string operator \hat{O}_{SPT} is not a consecutive product, and will decay exponentially at the SSB-PM transition. The symmetry-enriched percolation at the SSB-SPT transition can be understood via the dual transformation of $p_x \leftrightarrow p_{zzx}$, so that the SPT string operator \hat{O}_{SPT} features a power law behavior with exponent $2\Delta_{\text{bcc}} = 2/3$ whereas the PM string operator \hat{O}_{SPT} decays exponentially, which fully explains the numerical results in Fig. 2(d).

To end this part, we would like to mention that the Majorana modes can be split into two sets, say, $\mathcal{S}_1 = \{\gamma_{2i-1}\}_{i=1}^L$ and $\mathcal{S}_2 = \{\gamma_{2i}\}_{i=1}^L$, such that any projective measurement in Eq. (4) contains one Majorana mode from \mathcal{S}_1 and the other from \mathcal{S}_2 . Therefore, the word-line orientability of the corresponding loop model is conserved [49]. As a result, there is no critical ‘‘Goldstone’’ phase in our case, in contrast to the completely packed loop model with crossings where the orientability symmetry is broken [51].

* The first two authors contributed equally.

† ls20@mails.tsinghua.edu.cn

‡ sjian@tulane.edu

- [1] I. M. Georgescu, S. Ashhab, and F. Nori, *Rev. Mod. Phys.* **86**, 153 (2014).
- [2] R. Blatt and C. F. Roos, *Nature Physics* **8**, 277 (2012).
- [3] E. Altman, K. R. Brown, G. Carleo, L. D. Carr, E. Demler, C. Chin, B. DeMarco, S. E. Economou, M. A. Eriksson, K.-M. C. Fu, M. Greiner, K. R. Hazzard, R. G. Hulet, A. J. Kollár, B. L. Lev, M. D. Lukin, R. Ma, X. Mi, S. Misra, C. Monroe, K. Murch, Z. Nazario, K.-K. Ni, A. C. Potter, P. Roushan, M. Saffman, M. Schleier-Smith, I. Siddiqi, R. Simmonds, M. Singh, I. Spielman, K. Temme, D. S. Weiss, J. Vučković, V. Vuletić, J. Ye, and M. Zwierlein, *PRX Quantum* **2**, 017003 (2021).
- [4] C. Noel, P. Niroula, D. Zhu, A. Risinger, L. Egan, D. Biswas, M. Cetina, A. V. Gorshkov, M. J. Gullans, D. A. Huse, *et al.*, *Nature Physics* **18**, 760 (2022).
- [5] M. P. Fisher, V. Khemani, A. Nahum, and S. Vijay, *Annual Review of Condensed Matter Physics* **14**, 335 (2023).
- [6] Z.-L. Xiang, S. Ashhab, J. Q. You, and F. Nori, *Rev. Mod. Phys.* **85**, 623 (2013).
- [7] S. Sang and T. H. Hsieh, *Phys. Rev. Res.* **3**, 023200 (2021).
- [8] Y. Bao, S. Choi, and E. Altman, *Annals of Physics* **435**, 168618 (2021), special issue on Philip W. Anderson.
- [9] A. Lavasani, Y. Alavirad, and M. Barkeshli, *Nature Physics* **17**, 342 (2021).
- [10] A. Lavasani, Y. Alavirad, and M. Barkeshli, *Phys. Rev. Lett.* **127**, 235701 (2021).
- [11] A. Lavasani, Z.-X. Luo, and S. Vijay, *Phys. Rev. B* **108**, 115135 (2023).
- [12] G.-Y. Zhu, N. Tantivasadakarn, and S. Trebst, Structured volume-law entanglement in an interacting, monitored majorana spin liquid, [arXiv:2303.17627](https://arxiv.org/abs/2303.17627) (2023).
- [13] K. Klocke, D. Simm, G.-Y. Zhu, S. Trebst, and M. Buchhold, Entanglement dynamics in monitored kitaev circuits: loop models, symmetry classification, and quantum lifshitz scaling, [arXiv:2409.02171](https://arxiv.org/abs/2409.02171) (2024).
- [14] R. Morral-Yepes, F. Pollmann, and I. Lovas, *Phys. Rev. B* **108**, 224304 (2023).
- [15] K. Klocke and M. Buchhold, *Phys. Rev. B* **106**, 104307 (2022).
- [16] Y. Kuno and I. Ichinose, *Phys. Rev. B* **107**, 224305 (2023).
- [17] A. Sriram, T. Rakovszky, V. Khemani, and M. Ippoliti, *Phys. Rev. B* **108**, 094304 (2023).
- [18] T. Orito, Y. Kuno, and I. Ichinose, *Phys. Rev. B* **109**, 224306 (2024).
- [19] Y. Kuno and I. Ichinose, Emergence symmetry protected topological phase in spatially tuned measurement-only circuit, [arXiv:2212.13142](https://arxiv.org/abs/2212.13142) (2022).
- [20] Z. Zhang, Y. Li, and T.-C. Lu, Long-range entanglement from spontaneous non-onsite symmetry breaking, [arXiv:2411.05004](https://arxiv.org/abs/2411.05004) (2024).
- [21] H. Sukeno, K. Ikeda, and T.-C. Wei, *Phys. Rev. B* **110**, 245102 (2024).
- [22] T.-C. Lu, Z. Zhang, S. Vijay, and T. H. Hsieh, *PRX Quantum* **4**, 030318 (2023).
- [23] T.-C. Lu, L. A. Lessa, I. H. Kim, and T. H. Hsieh, *PRX Quantum* **3**, 040337 (2022).
- [24] Y. Li, X. Chen, and M. P. A. Fisher, *Phys. Rev. B* **98**, 205136 (2018).
- [25] Y. Li, X. Chen, and M. P. A. Fisher, *Phys. Rev. B* **100**, 134306 (2019).
- [26] C.-M. Jian, Y.-Z. You, R. Vasseur, and A. W. W. Ludwig, *Phys. Rev. B* **101**, 104302 (2020).
- [27] R. Vasseur, A. C. Potter, Y.-Z. You, and A. W. W. Ludwig, *Phys. Rev. B* **100**, 134203 (2019).
- [28] B. Skinner, J. Ruhman, and A. Nahum, *Phys. Rev. X* **9**, 031009 (2019).
- [29] S. Choi, Y. Bao, X.-L. Qi, and E. Altman, *Phys. Rev. Lett.* **125**, 030505 (2020).
- [30] S.-K. Jian, C. Liu, X. Chen, B. Swingle, and P. Zhang, *Phys. Rev. Lett.* **127**, 140601 (2021).
- [31] Y. Bao, S. Choi, and E. Altman, *Phys. Rev. B* **101**, 104301 (2020).
- [32] X. Turkeshi, A. Biella, R. Fazio, M. Dalmonte, and M. Schiró, *Phys. Rev. B* **103**, 224210 (2021).
- [33] N. Lang and H. P. Büchler, *Phys. Rev. B* **102**, 094204 (2020).
- [34] M. Ippoliti, M. J. Gullans, S. Gopalakrishnan, D. A. Huse, and V. Khemani, *Phys. Rev. X* **11**, 011030 (2021).
- [35] M. Buchhold, Y. Minoguchi, A. Altland, and S. Diehl, *Phys. Rev. X* **11**, 041004 (2021).
- [36] Q. Tang and W. Zhu, *Phys. Rev. Res.* **2**, 013022 (2020).
- [37] T. Müller, S. Diehl, and M. Buchhold, *Phys. Rev. Lett.* **128**, 010605 (2022).
- [38] T. Minato, K. Sugimoto, T. Kuwahara, and K. Saito, *Phys. Rev. Lett.* **128**, 010603 (2022).
- [39] A. Nahum, S. Roy, B. Skinner, and J. Ruhman, *PRX Quantum* **2**, 010352 (2021).
- [40] M. Tikhonovskaya, A. Lavasani, M. P. A. Fisher, and S. Vijay, *Phys. Rev. B* **109**, 224313 (2024).
- [41] T.-C. Lu, *Phys. Rev. B* **110**, 125145 (2024).

- [42] X. Turkeshi, *Phys. Rev. B* **106**, 144313 (2022).
- [43] S. Liu, M.-R. Li, S.-X. Zhang, S.-K. Jian, and H. Yao, *Phys. Rev. B* **110**, 064323 (2024).
- [44] T.-C. Lu and T. Grover, *PRX Quantum* **2**, 040319 (2021).
- [45] W. Wang, S. Liu, J. Li, S.-X. Zhang, and S. Yin, Driven critical dynamics in measurement-induced phase transitions, [arXiv:2411.06648](https://arxiv.org/abs/2411.06648) (2024).
- [46] A.-R. Negari, S. Sahu, and T. H. Hsieh, *Phys. Rev. B* **109**, 125148 (2024).
- [47] S. Liu, M.-R. Li, S.-X. Zhang, and S.-K. Jian, *Phys. Rev. Lett.* **132**, 240402 (2024).
- [48] S. Liu, M.-R. Li, S.-X. Zhang, S.-K. Jian, and H. Yao, *Phys. Rev. B* **107**, L201113 (2023).
- [49] K. Klocke and M. Buchhold, *Phys. Rev. X* **13**, 041028 (2023).
- [50] A. Nahum and B. Skinner, *Phys. Rev. Res.* **2**, 023288 (2020).
- [51] A. Nahum, P. Serna, A. M. Somoza, and M. Ortuño, *Phys. Rev. B* **87**, 184204 (2013).
- [52] S. Sang, Y. Li, T. Zhou, X. Chen, T. H. Hsieh, and M. P. Fisher, *PRX Quantum* **2**, 030313 (2021).
- [53] P. Zhang, C. Liu, S.-K. Jian, and X. Chen, *Quantum* **6**, 723 (2022).
- [54] P. Zhang, S.-K. Jian, C. Liu, and X. Chen, *Quantum* **5**, 579 (2021).
- [55] S.-K. Jian, Z.-C. Yang, Z. Bi, and X. Chen, *Phys. Rev. B* **104**, L161107 (2021).
- [56] X. Feng, S. Liu, S. Chen, and W. Guo, *Phys. Rev. B* **107**, 094309 (2023).
- [57] D. Qian and J. Wang, [arXiv:2406.14109](https://arxiv.org/abs/2406.14109) (2024).
- [58] M. Cheng and H.-H. Tu, *Phys. Rev. B* **84**, 094503 (2011).
- [59] L. Fidkowski, R. M. Lutchyn, C. Nayak, and M. P. A. Fisher, *Phys. Rev. B* **84**, 195436 (2011).
- [60] J. P. Kestner, B. Wang, J. D. Sau, and S. Das Sarma, *Phys. Rev. B* **83**, 174409 (2011).
- [61] A. Keselman and E. Berg, *Phys. Rev. B* **91**, 235309 (2015).
- [62] J. Ruhman and E. Altman, *Phys. Rev. B* **96**, 085133 (2017).
- [63] D. E. Parker, T. Scaffidi, and R. Vasseur, *Phys. Rev. B* **97**, 165114 (2018).
- [64] H.-C. Jiang, Z.-X. Li, A. Seidel, and D.-H. Lee, *Science Bulletin* **63**, 753 (2018).
- [65] A. Keselman, E. Berg, and P. Azaria, *Phys. Rev. B* **98**, 214501 (2018).
- [66] T. Scaffidi, D. E. Parker, and R. Vasseur, *Phys. Rev. X* **7**, 041048 (2017).
- [67] R. Thorngren, A. Vishwanath, and R. Verresen, *Phys. Rev. B* **104**, 075132 (2021).
- [68] R. Verresen, R. Thorngren, N. G. Jones, and F. Pollmann, *Phys. Rev. X* **11**, 041059 (2021).
- [69] R. Verresen, Topology and edge states survive quantum criticality between topological insulators, [arXiv:2003.05453](https://arxiv.org/abs/2003.05453) (2020).
- [70] C. M. Duque, H.-Y. Hu, Y.-Z. You, V. Khemani, R. Verresen, and R. Vasseur, *Phys. Rev. B* **103**, L100207 (2021).
- [71] X.-J. Yu, R.-Z. Huang, H.-H. Song, L. Xu, C. Ding, and L. Zhang, *Phys. Rev. Lett.* **129**, 210601 (2022).
- [72] X.-J. Yu, S. Yang, H.-Q. Lin, and S.-K. Jian, *Phys. Rev. Lett.* **133**, 026601 (2024).
- [73] D. E. Parker, R. Vasseur, and T. Scaffidi, *Phys. Rev. Lett.* **122**, 240605 (2019).
- [74] X.-J. Yu and W.-L. Li, *Phys. Rev. B* **110**, 045119 (2024).
- [75] S. Yang, H.-Q. Lin, and X.-J. Yu, Gifts from long-range interaction: Emergent gapless topological behaviors in quantum spin chain, [arXiv:2406.01974](https://arxiv.org/abs/2406.01974) (2024).
- [76] W.-H. Zhong, W.-L. Li, Y.-C. Chen, and X.-J. Yu, *Phys. Rev. A* **110**, 022212 (2024).
- [77] U. Borla, R. Verresen, J. Shah, and S. Moroz, *SciPost Phys.* **10**, 148 (2021).
- [78] A. J. Friedman, B. Ware, R. Vasseur, and A. C. Potter, *Phys. Rev. B* **105**, 115117 (2022).
- [79] L. Li, M. Oshikawa, and Y. Zheng, Intrinsically/purely gapless-spt from non-invertible duality transformations (2023), [arXiv:2307.04788](https://arxiv.org/abs/2307.04788) (2023).
- [80] S.-J. Huang and M. Cheng, Topological holography, quantum criticality, and boundary states, [arXiv:2310.16878](https://arxiv.org/abs/2310.16878) (2023).
- [81] R. Wen and A. C. Potter, *Phys. Rev. B* **107**, 245127 (2023).
- [82] R. Wen and A. C. Potter, Classification of 1+1d gapless symmetry protected phases via topological holography, [arXiv:2311.00050](https://arxiv.org/abs/2311.00050) (2023).
- [83] R. Wen, String condensation and topological holography for 2+1d gapless spt, [arXiv:2408.05801](https://arxiv.org/abs/2408.05801) (2024).
- [84] L. Li, M. Oshikawa, and Y. Zheng, *SciPost Phys.* **17**, 013 (2024).
- [85] S.-J. Huang, Fermionic quantum criticality through the lens of topological holography, [arXiv:2405.09611](https://arxiv.org/abs/2405.09611) (2024).
- [86] L. Su and M. Zeng, *Phys. Rev. B* **109**, 245108 (2024).
- [87] H.-L. Zhang, H.-Z. Li, S. Yang, and X.-J. Yu, *Phys. Rev. A* **109**, 062226 (2024).
- [88] T. Ando, S. Ryu, and M. Watanabe, Gauge theory and mixed state criticality, [arXiv:2411.04360](https://arxiv.org/abs/2411.04360) (2024).
- [89] L. Zhou, J. Gong, and X.-J. Yu, Topological edge states at floquet quantum criticality, [arXiv:2410.15395](https://arxiv.org/abs/2410.15395) (2024).
- [90] L. Li, R.-Z. Huang, and W. Cao, Noninvertible symmetry-enriched quantum critical point, [arXiv:2411.19034](https://arxiv.org/abs/2411.19034) (2024).
- [91] X.-G. Wen, *Rev. Mod. Phys.* **89**, 041004 (2017).
- [92] Z.-C. Gu and X.-G. Wen, *Phys. Rev. B* **80**, 155131 (2009).
- [93] X. Chen, Z.-C. Gu, and X.-G. Wen, *Phys. Rev. B* **83**, 035107 (2011).
- [94] X. Chen, Z.-C. Gu, Z.-X. Liu, and X.-G. Wen, *Science* **338**, 1604 (2012).
- [95] J. L. Cardy, *Journal of Physics A: Mathematical and General* **25**, L201 (1992).
- [96] J. Cardy, Conformal invariance and percolation, [arXiv:math-ph/0103018](https://arxiv.org/abs/math-ph/0103018) (2001).
- [97] It can be understood by a symmetry breaking transition for τ spins from the Phase II due to the $\tau_{2i-1}^x \tau_{2i+1}^x$ perturbation, or by a symmetry restoration for σ spins from the Phase III due to the increase in the σ^x measurements.
- [98] P. Fendley and J. L. Jacobsen, *Journal of Physics A: Mathematical and Theoretical* **41**, 215001 (2008).
- [99] D. Fattal, T. S. Cubitt, Y. Yamamoto, S. Bravyi, and I. L. Chuang, [arXiv preprint quant-ph/0406168](https://arxiv.org/abs/quant-ph/0406168) (2004).
- [100] A. Nahum, J. Ruhman, S. Vijay, and J. Haah, *Phys. Rev. X* **7**, 031016 (2017).
- [101] J. L. Jacobsen and H. Saleur, *Phys. Rev. Lett.* **100**, 087205 (2008).
- [102] H. N. V. Temperley and E. H. Lieb, Relations between the ‘percolation’ and ‘colouring’ problem and

- other graph-theoretical problems associated with regular planar lattices: some exact results for the ‘percolation’ problem, in *Condensed Matter Physics and Exactly Soluble Models: Selecta of Elliott H. Lieb*, edited by B. Nachtergaele, J. P. Solovej, and J. Yngvason (Springer Berlin Heidelberg, Berlin, Heidelberg, 2004) pp. 475–504.
- [103] B. Zeng, X. Chen, D.-L. Zhou, X.-G. Wen, *et al.*, *Quantum information meets quantum matter* (Springer, 2019).
- [104] M. Levin and Z.-C. Gu, *Phys. Rev. B* **86**, 115109 (2012).
- [105] S. R. White, *Phys. Rev. Lett.* **69**, 2863 (1992).
- [106] S. R. White, *Phys. Rev. B* **48**, 10345 (1993).
- [107] U. Schollwöck, *Annals of Physics* **326**, 96 (2011), january 2011 Special Issue.

Supplemental Material for “Gapless Symmetry-Protected Topological States in Measurement-Only Circuits”

CONTENTS

I. Observables in measurement-only quantum circuits	10
II. Additional results for the Ising cluster circuit model	11
A. Steady state phase diagram via the order parameters	11
B. Determination of the critical points for the case of $p_x = 0.2$ and $p_x = 0.4$	11
C. Purification dynamics on the symmetry-enriched percolation line for $p_x \neq 0$	12
D. Different behaviors of the string operators at the topologically trivial and nontrivial critical points	12
III. Additional results for the \mathbb{Z}_4 symmetric circuit model	14
A. The equilibrium ground-state phase diagram	14
B. Simulation results for the case of $p_h = p_\delta$	15
C. Simulation results for spin-spin correlations	15
D. Effect of the single-site measurement τ_{2i-1}^x on the \mathbb{Z}_4 symmetric circuit model	16

I. OBSERVABLES IN MEASUREMENT-ONLY QUANTUM CIRCUITS

In this section, we introduce the physical observables utilized in the main text to investigate the steady state of measurement-only circuits.

Half-chain entanglement entropy. For the state $|\psi_t\rangle$ evolved after t discrete time steps, we can calculate the von Neumann entanglement entropy,

$$S_R = -\text{Tr}(\rho_R \log_2 \rho_R), \quad (\text{S1})$$

where ρ_R is the reduced density matrix of the subregion R of the system and S_R quantifies the entanglement between the subsystem R and its complement \bar{R} . Then the most common observable in measurement-only circuits, the half-chain entanglement entropy, is defined by $S_{\text{Half}} \equiv S_{\mathcal{L}}$ with $\mathcal{L} = \{1, \dots, L/2\}$, whose size-scaling behaviors can be used to classify the steady states into area-law or volume-law entangled phases and to detect the entanglement phase transitions. In particular, for the percolation-type phase transition relevant in measurement-only circuits, it has been investigated that the ensemble averaged S_{Half} at the criticality exhibits a logarithmic scaling with the system size L [49], namely, $S_{\text{Half}}(L) = c_{\text{eff}} \log_2 L + c'$, where the prefactor c_{eff} which we call the effective central charge has an exact value $\sqrt{3} \ln 2 / (4\pi)$ under open boundary conditions and c' is a non-universal constant.

Generalized topological entropy. Another entanglement quantity relevant in our work is the generalized topological entanglement entropy S_{topo} which can be used to characterize the nontrivial topology of the evolved state $|\psi_t\rangle$. By partitioning the whole system into four subregions with equal size, $A|B|D|C$ [see Fig. 2(a) in the main text], S_{topo} is defined by [103]

$$S_{\text{topo}} \equiv S_{AB} + S_{BC} - S_B - S_{ABC}. \quad (\text{S2})$$

For example, it is known that $S_{\text{topo}} = 2$ within the $\mathbb{Z}_2 \times \mathbb{Z}_2$ (cluster) symmetry-protected topological (SPT) phase while $S_{\text{topo}} = 0$ in the spontaneous symmetry-breaking (SSB) phase. Therefore, S_{topo} can faithfully distinguish between the SPT and SSB phases, as well as locate the corresponding critical point [9].

Order parameters. Besides the entanglement observables enumerated above, some recent works [7, 14] show that conventional order parameters can also be used to characterize the long-range orders stabilized by the quantum circuit with suitable modifications. For the Ising cluster circuit model, we can define three order parameters to detect the possible existence of the paramagnetic (PM), SSB, and SPT orders

$$O_{\text{SSB}}(i, j) = \overline{|\langle Z_i Z_j \rangle|}, \quad (\text{S3})$$

$$O_{\text{PM}}(i, j) = \overline{|\langle X_i X_{i+1} \cdots X_{j-1} X_j \rangle|}, \quad (\text{S4})$$

$$O_{\text{SPT}}(i, j) = \overline{|\langle Z_{i-1} Y_i X_{i+1} \cdots X_{j-1} Y_j Z_{j+1} \rangle|}, \quad (\text{S5})$$

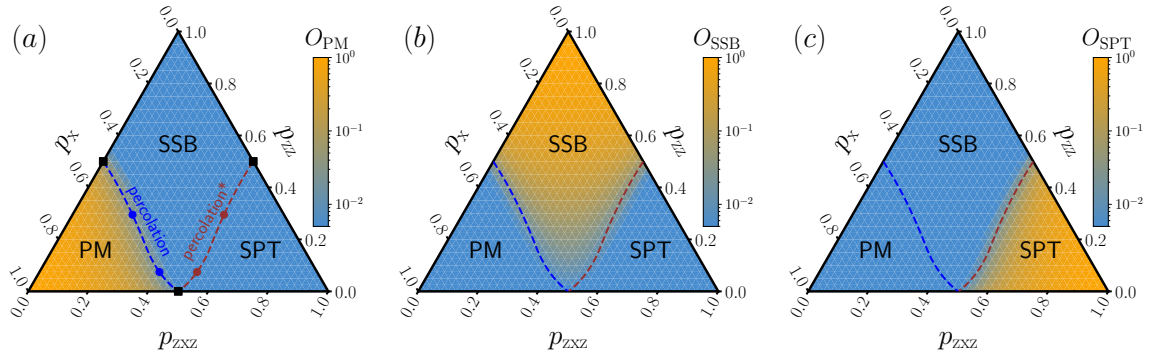


FIG. S1. Order parameters, (a) O_{PM} , (b) O_{SSB} , and (c) O_{SPT} , shown as a function of the measurement probabilities p_x , p_{zz} , and p_{zzz} , simulated with system size $L = 96$ under open boundary conditions. The black squares are exact critical points when only two types of measurements are present. The red circles are critical points obtained by the data collapse of the generalized topological entanglement entropy (see Fig. S2) and the red dashed line is a guide to the eye. The blue circles and the corresponding dashed line are obtained by $p_x \leftrightarrow p_{zzz}$.

where, in practical simulations, one can choose $i = L/4 + 1$ and $j = 3L/4$ to reduce the possible boundary effect under the open boundary condition. Different from the conventional definitions used in the equilibrium case, here, the observables are ensemble averaged over many different trajectory realizations and the module before the average is necessary to obtain meaningful (nonzero) results [14]. For the \mathbb{Z}_4 symmetric circuit model, similar order parameters can be defined as shown in Section III of the Supplemental Material.

II. ADDITIONAL RESULTS FOR THE ISING CLUSTER CIRCUIT MODEL

A. Steady state phase diagram via the order parameters

In the main text, the phase transition between the SPT and SSB phases has been investigated mainly in the case of no X_i measurement, namely, $p_x = 0$. Here, we aim to consider the case where all three types of measurements are present and try to map out the phase diagram of the steady state in the whole parameter space (p_x, p_{zz}, p_{zzz}) . It is noted that previous works have studied the cases of $p_{zzz} = 0$ [7, 9] and $p_{zz} = 0$ [14]. It was observed that there is a phase transition between the SSB and trivial PM phases in the former and a transition between the SPT and PM phases in the latter; both transitions happen when the two relevant measurement probabilities are tuned to be equal. However, when all three types of measurements are present in the circuit, the situation becomes more complex and the phase diagram has not been figured out before.

To map out the steady-state phase diagram, we first calculate the three order parameters, O_{PM} , O_{SSB} , and O_{SPT} , within the whole parameter regime as displayed in Fig. S1. It is obvious that the phase diagram is roughly partitioned into three regions: SSB, PM, and SPT. The result supports the stability of these three phases in the presence of all three competing measurements.

B. Determination of the critical points for the case of $p_x = 0.2$ and $p_x = 0.4$

Our next task is to determine the location of the transition lines between the different phases. Similar to the duality argument given in Ref. [9], it is noted that the structure of the phase diagram should be symmetric for $p_x \leftrightarrow p_{zzz}$ under the global unitary transformation $U_{\text{SPT}} = \prod_{i=1}^L \text{CZ}_{i,i+1}$ (here $\text{CZ}_{i,i+1}$ is the two-qubit controlled-Z gate) which transforms X_i into $Z_{i-1}X_iZ_{i+1}$ and vice versa; periodic boundary condition is assumed here. Since U_{SPT} transforms local stabilizers to local stabilizers, the state in an area-law entangled phase still obeys the area law after the transformation [9]. As a result, if a continuous phase transition occurs at (p_x, p_{zz}, p_{zzz}) with logarithmic entanglement entropy, we can find another corresponding phase transition intermediately by $p_x \leftrightarrow p_{zzz}$. We also notice that this symmetry becomes transparent in the Majorana representation as illustrated in Fig. 5 in the Appendix. Therefore, it is sufficient to locate the transition line between SPT and SSB, and the other one can be inferred simply by $p_x \leftrightarrow p_{zzz}$.

In the main text, we have evidenced that the generalized topological entanglement entropy S_{topo} is a powerful tool

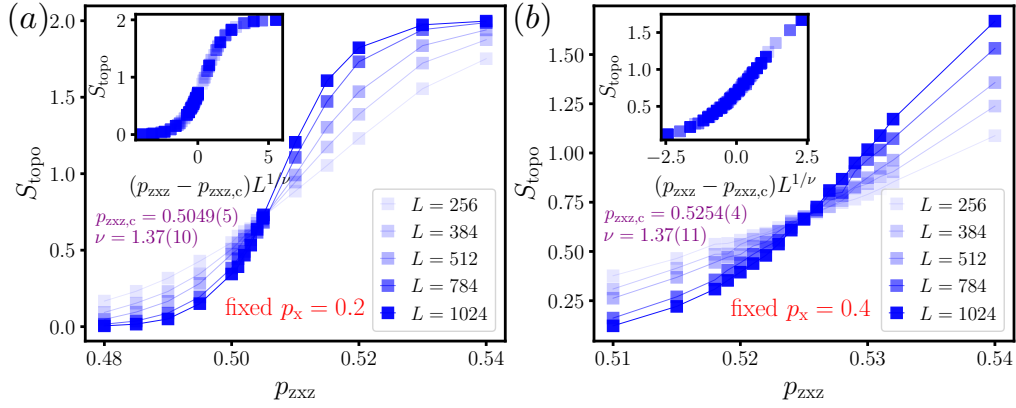


FIG. S2. The generalized topological entanglement entropy S_{topo} versus the measurement probability p_{zzz} for various system sizes with (a) $p_x = 0.2$ and (b) $p_x = 0.4$, respectively. The insets exhibit the data collapses of S_{topo} with $p_{\text{zzz},c} = 0.5049(5)$ and $\nu = 1.37(10)$ for $p_x = 0.2$ and $p_{\text{zzz},c} = 0.5254(4)$ and $\nu = 1.37(11)$ for $p_x = 0.4$, respectively.

to study the SPT-SSB transition. By fixing $p_x = 0.2$, we have computed the ensemble average of S_{topo} as a function of p_{zzz} as exhibited in Fig. S2(a). It is shown that curves of different system sizes cross at a single point suggesting the existence of a phase transition. The data collapse further determines the transition point $p_{\text{zzz},c} = 0.5049(5)$ and the critical exponent $\nu = 1.37(10)$. Similar analysis for the case of $p_x = 0.4$ also gives the estimation $p_{\text{zzz},c} = 0.5254(4)$ and $\nu = 1.37(11)$. Together with the logarithmic half-chain entanglement entropy displayed in Fig. 2(b) in the main text, it implies that adding a finite probability of X_i measurement does not change the bond percolation universality class of the SPT-SSB transition.

C. Purification dynamics on the symmetry-enriched percolation line for $p_x \neq 0$

In this section, we performed additional numerical simulations for the purification dynamics at the symmetry-enriched percolation critical points in the case of $p_x = 0.2$ and $p_x = 0.4$. By starting from a maximally mixed state, the initial entanglement entropy of the full system is $S(t=0) = L$ and the entanglement entropy will decrease as time increases as the projective measurements can purify the state. As presented in Fig. S3, in the late-time regime, we can fit the residue entropy $S(t) \sim e^{-t/\tau}$ and the fitted τ is found satisfying $\tau \sim L^z$ where $z = 1.008$ is the dynamical exponent. The data collapse in the inset indicates that the residue entropy of the full system is always nonzero at finite times in the thermodynamic limit. It means that there is an encoded subspace that survives for arbitrarily long times when $L \rightarrow \infty$, providing potential evidence for the existence of the edge modes on the symmetry-enriched percolation line. Numerical simulations for the case of $p_x = 0.4$ have also been performed and similar results are obtained as displayed in Figs. S4.

D. Different behaviors of the string operators at the topologically trivial and nontrivial critical points

Finally, we compare the scaling behaviors of the relevant string order parameters $O_{\text{SPT}}(r)$ and $O_{\text{PM}}(r)$ at the critical points $p_x = p_{\text{zz}} = 1/2$ and $p_{\text{zz}} = p_{\text{zzz}} = 1/2$, respectively. As shown in Fig. S5, $O_{\text{SPT}}(r)$ exhibits a power-law decay with respect to the site distance r at the symmetry-enriched percolation critical point, while $O_{\text{PM}}(r)$ decays much faster than $O_{\text{SPT}}(r)$ at this point. However, at the trivial percolation criticality, the situation is reversed, and $O_{\text{SPT}}(r)$ decays significantly faster than $O_{\text{PM}}(r)$. This result provides further evidence for the topological distinction between the two percolation critical lines shown in Fig. 1(b) in the main text.

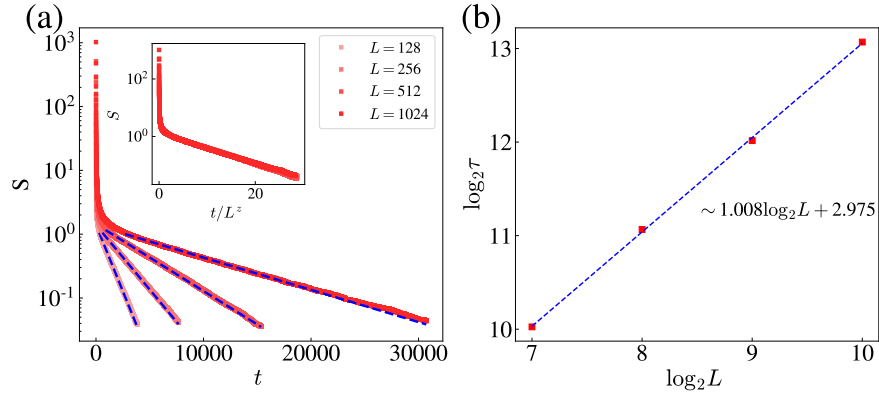


FIG. S3. (a) The entanglement entropy of the whole system S as a function of the evolving time t for various system sizes at the estimated critical point $p_x = 0.2$ and $p_{zxx} = 0.5049$. The initial state is the maximally mixed state. The dashed blue line represents the fitting $S(t) \sim e^{-t/\tau}$ using the late-time data. Inset shows the data collapse of $S(t)$ with rescaled x-axis t/L^z where z is given by $\tau \sim L^z$. (b) shows the least-squares fitting of $\tau \sim L^z$, which gives $z \approx 1.008$.

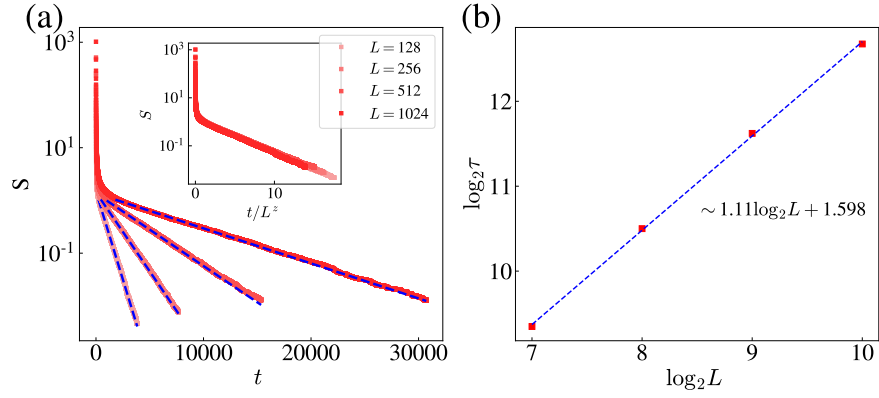


FIG. S4. (a) The dynamics of the entanglement entropy of the whole system S starting from the maximally mixed state for different system sizes at the estimated critical point $p_x = 0.4$ and $p_{zxx} = 0.5254$. The dashed blue line represents the fitting $S(t) \sim e^{-t/\tau}$ using the late-time part of the data. Inset shows the data collapse with rescaled x-axis t/L^z where z is given by $\tau \sim L^z$. (b) displays the least-squares fitting $\tau \sim L^z$, which gives $z \approx 1.11$.

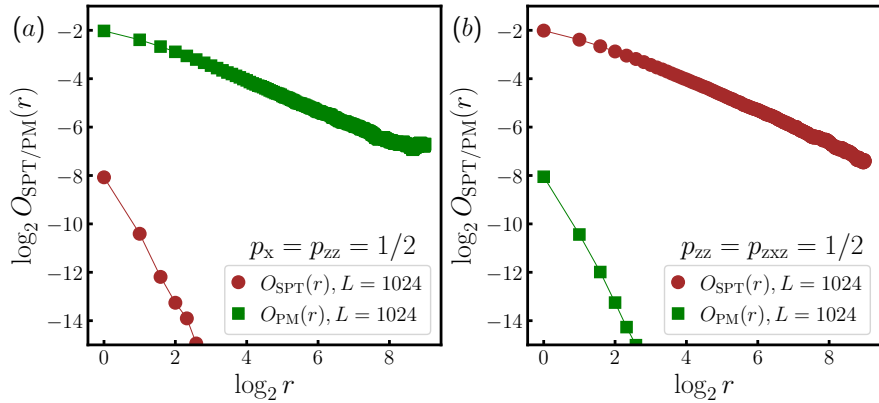


FIG. S5. String order parameters, $O_{\text{SPT}}(r)$ (red circles) and $O_{\text{PM}}(r)$ (green squares), as a function of the site distance r for (a) $p_x = p_{zz} = 1/2$ and (b) $p_{zz} = p_{zxx} = 1/2$, respectively. The simulated system size is $L = 1024$ under open boundary conditions.

III. ADDITIONAL RESULTS FOR THE \mathbb{Z}_4 SYMMETRIC CIRCUIT MODEL

A. The equilibrium ground-state phase diagram

First, we recall the physics in the equilibrium case for later comparison with its non-equilibrium counterpart. The model is a quantum spin chain with two $1/2$ spins per unit cell, which is described by the following Hamiltonian,

$$H_{\text{igSPT}} = - \sum_{i=1}^L (\tau_{2i-1}^z \sigma_{2i}^x \tau_{2i+1}^z + \tau_{2i-1}^y \sigma_{2i}^x \tau_{2i+1}^y + \sigma_{2i}^z \tau_{2i+1}^x \sigma_{2i+2}^z). \quad (\text{S6})$$

This model is obtained by stacking an Ising (\mathbb{Z}_2 SSB) spin chain with an XX Hamiltonian,

$$H_{\text{Ising+XX}} = - \sum_{i=1}^L (\tau_{2i-1}^z \tau_{2i+1}^z + \tau_{2i-1}^y \tau_{2i+1}^y) - \sum_{i=1}^L \sigma_{2i}^z \sigma_{2i+2}^z, \quad (\text{S7})$$

through the Kennedy-Tasaki (KT) transformation [79]. Since the Ising chain and the XX chain is completely decoupled in $H_{\text{Ising+XX}}$, we can easily read off the spin-spin correlation functions

$$\langle \sigma_{2i}^z \sigma_{2j}^z \rangle = 1, \quad \langle \tau_{2i-1}^z \tau_{2j-1}^z \rangle \sim 1/|i-j|^\Delta, \quad (\text{S8})$$

where $\Delta/2$ is the scaling dimension of τ^z . These conventional correlations then become the string order parameters after the KT transformation

$$O_\sigma(r = |i-j|) = \langle \sigma_{2i}^z (\prod_{k=i}^{j-1} \tau_{2k+1}^x) \sigma_{2j}^z \rangle = 1, \quad O_\tau(r = |i-j|) = \langle \tau_{2i-1}^z (\prod_{k=i}^{j-1} \sigma_{2k}^x) \tau_{2j-1}^z \rangle \sim 1/|i-j|^\Delta. \quad (\text{S9})$$

These nonlocal string operators characterize the nontrivial topology of the intrinsic gSPT phase. More specifically, the system possesses a \mathbb{Z}_4 symmetry generated by $U = \prod_i \sigma_{2i}^x e^{i\frac{\pi}{4}(1-\tau_{2i-1}^x)}$, which exhibits an emergent anomaly at low energies that is the same anomaly on the boundary of a 2+1D Levin-Gu SPT state [104]. One can see easily that, under the open boundary condition, the square of U fractionalizes onto each end of the boundary as $U^2 \sim \tau_1^x \sigma_2^z \sigma_{2L}^z$ [81, 82]. It is also noted that the gSPT phase is robust against the symmetric perturbation by adding $\delta \sum_i \tau_{2i-1}^x \tau_{2i+1}^x$ when $|\delta| < 1$ or $h \sum_i \sigma_{2i}^x$ when $|h| < 1$; the ground-state phase diagram in the presence of both perturbations is mapped out in Fig. S6. It motivates us to investigate the steady state phase diagram of the \mathbb{Z}_4 symmetric measurement-only circuit including the corresponding two-site and one-site projective measurement perturbations. The resulting non-equilibrium phase diagram is displayed in Fig. 3(a1) in the main text.

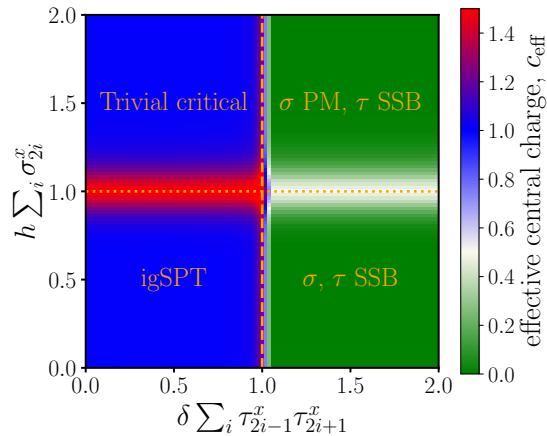


FIG. S6. The ground-state phase diagram of the Hamiltonian, $H_{\text{igSPT}} - \delta \sum_i \tau_{2i-1}^x \tau_{2i+1}^x - h \sum_i \sigma_{2i}^x$, as a function of h and δ is mapped out by calculating the effective central charge c_{eff} , where c_{eff} is estimated by fitting to $S(l) = \frac{c_{\text{eff}}}{3} \log_2(L/\pi \sin[\pi l/L]) + \text{const}$. The dotted line ($h = 1$) is an Ising transition while the dashed line ($\delta = 1$) is a BKT transition. Simulation is performed by exploiting the density matrix renormalization group algorithm [105–107] with $L = 24$ under periodic boundary conditions.

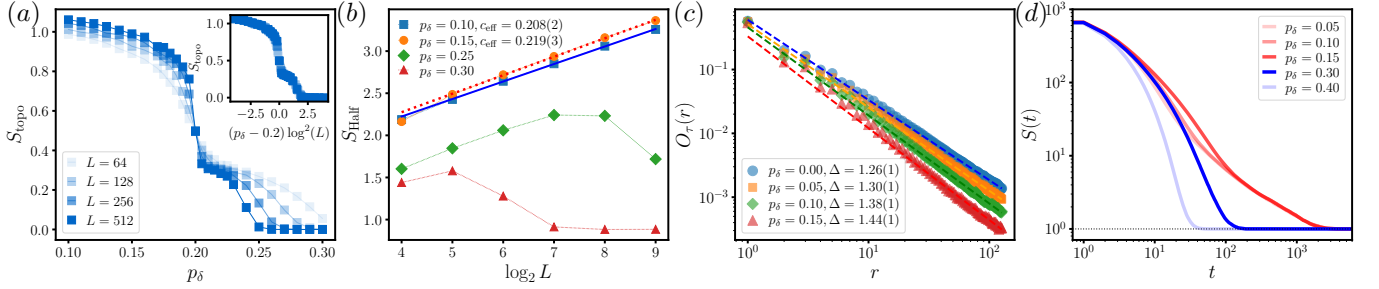


FIG. S7. The simulation result for the \mathbb{Z}_4 symmetric circuit model in the case of $p_h = p_\delta$ crossing the special point $p_h = p_\delta = 1/5$. (a) The data collapse of the generalized topological entanglement entropy S_{topo} with the rescaled x-axis $(p_\delta - 0.2) \log^2(L)$ using the critical point $p_{\delta,c} = 1/5$. (b) The finite-size scaling of the half-chain entanglement entropy S_{Half} shows logarithmic growth for $p_\delta < 1/5$. The blue solid and orange dotted lines are least-squares fittings giving the estimated effective central charges $c_{\text{eff}} = 0.208(2)$ and $c_{\text{eff}} = 0.219(3)$, respectively. (c) The string order parameter $O_\tau(r)$ as a function of the site distance r for different $p_\delta < 1/5$. (d) The dynamics of the full system entropy $S(t)$ versus the evolution time t for different values of p_δ . The simulated system size is $L = 256$ for (c) and $L = 512$ for (d) under open boundary conditions.

B. Simulation results for the case of $p_h = p_\delta$

In the main text, we have investigated the physics of the steady state of the \mathbb{Z}_4 symmetric circuit model along the horizontal $p_h = 0.0$ line and the vertical $h_\delta = 0.08$ line. Here, we provide additional results for the case of $p_h = p_\delta$ which includes the crossing point of the BKT and percolation transition lines, namely, $p_h = p_\delta = 1/5$.

As displayed in Fig. S7(a), we calculate the generalized topological entanglement entropy S_{topo} for different system sizes near the critical point; a perfect data collapse is achieved by using $p_{\delta,c} = 1/5$ with a standard logarithmic-squared scaling form for BKT transitions. It is noted that the coexisting percolation transition is invisible in the finite-size scaling analysis due to the BKT transition. By further investigating the system-size dependence of the half-chain entanglement entropy S_{Half} , we can clearly see that S_{Half} shows a logarithmic growth with L at $p_\delta = 0.10$ and $p_\delta = 0.15$ (belongs to the gSPT phase) as shown in Fig. S7(b). The fitted effective central charge c_{eff} is also close to $2 \times \frac{\sqrt{3} \ln 2}{4\pi}$. The parameter regime $p_\delta > 1/5$ is an (a) SSB (PM) in the τ (σ) degrees of freedom, which shows an area-law S_{Half} when L is large enough. This observation is also supported by examining the asymptotic behavior of the string order parameter $O_\tau(r)$ as plotted in Fig. S7(c). It is clear that $O_\tau(r)$ exhibits a power-law decaying behavior with an exponent $\Delta \approx 4/3$ for $p_\delta < 1/5$ supporting the existence of a stable gSPT phase. Finally, we can see a nonzero residue entropy $S(t \gg L) = 1$ in the purification dynamics for both $p_\delta < 1/5$ and $p_\delta > 1/5$ as shown in Fig. S7(d). The nontrivial residue entropy comes from the topological protected edge modes in the gSPT phase for $p_\delta < 1/5$ and the SSB in the τ degrees of freedom for $p_\delta > 1/5$, respectively.

In summary, the numerical results shown here agree with the observation in the main text and can help us to check the correctness of the predicted BKT (percolation) line $p_h + 4p_\delta = 1$ ($4p_h + p_\delta = 1$) in the steady-state phase diagram shown in Fig. 3(a1) in the main text.

C. Simulation results for spin-spin correlations

To support the analyses and the conclusions made in the main text, we perform simulations to calculate the spin-spin correlations respectively for σ and τ degrees of freedom. In particular, we investigate the following (connected) correlations

$$C_\sigma^z(r) = \overline{|\langle \sigma_2^z \sigma_{2+2r}^z \rangle|}, \quad C_\tau^x(r) = \overline{|\langle \tau_1^x \tau_{1+2r}^x \rangle|}, \quad \tilde{C}_\tau^x(r) = \overline{|\langle \tau_1^x \tau_{1+2r}^x \rangle - \langle \tau_1^x \rangle \langle \tau_{1+2r}^x \rangle|}, \quad (\text{S10})$$

at representative points for each phase shown in Fig. 3(a1) in the main text. We do not consider the connected σ^z correlation as the expectation $\langle \sigma_i^z \rangle$ is zero for all i which is guaranteed by the symmetry of the circuit dynamics.

As displayed in Fig. S8, the spin-spin correlations show different behaviors among the chosen points. For $p_h = p_\delta = 0.08$ in the Phase I, both $C_\sigma^z(r)$ and $C_\tau^x(r)$ display power-law decaying behaviors due to the critical τ degrees of freedom. When we add the one-site perturbation and drive the system into the Phase II (e.g., $p_h = 0.45$ and $p_\delta = 0.08$), the τ degrees of freedom are still critical while the σ degrees of freedom are trivially gapped leading to an exponentially decaying $C_\sigma^z(r)$. On the other hand, when we add the two-site perturbation and drive the system into

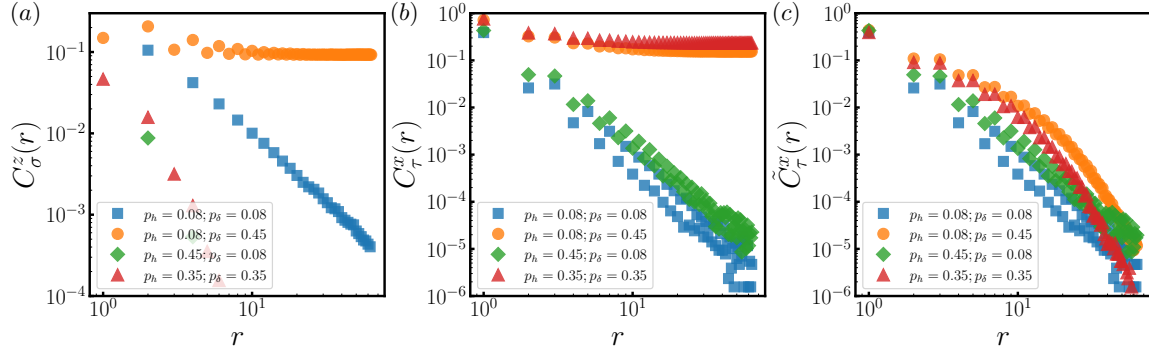


FIG. S8. Spin-spin correlations (a) $C_\sigma^z(r)$ and (b) $C_\tau^x(r)$ versus the site distance r for four representative parameter points in the steady-state phase diagram. (c) The connected correlation $\tilde{C}_\tau^x(r)$ as a function of r for the same parameters. Simulations are performed with a system of size $L = 128$ under open boundary conditions.

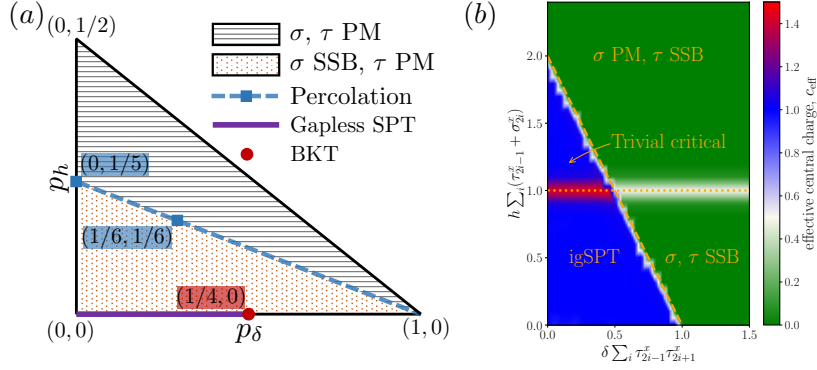


FIG. S9. (a) The steady state phase diagram of the \mathbb{Z}_4 symmetric circuit including the single-site perturbation τ_{2i-1}^x with the same occurring probability as σ_{2i}^x ; it is noted that $3p_t + p_\delta + 2p_h = 1$. The percolation transition line (blue dashed) is $5p_h + p_\delta = 1$. (b) The corresponding ground-state phase diagram of the Hamiltonian, $H_{\text{igSPT}} - \delta \sum_i \tau_{2i-1}^x \tau_{2i+1}^x - h \sum_i (\tau_{2i-1}^x + \sigma_{2i}^x)$, is obtained from calculating the effective central charge c_{eff} . The dotted line ($h = 1$) is an Ising transition while the dashed line ($2\delta + h = 2$) is a BKT transition. Simulation is performed by exploiting the density matrix renormalization group algorithm with $L = 48$ under periodic boundary conditions.

the Phase III (e.g., $p_h = 0.08$ and $p_\delta = 0.45$), the τ degrees of freedom are gapped out resulting in a long-range SSB order in the x (z) direction of the τ (σ) spins. Finally, for $p_h = p_\delta = 0.45$ in the Phase IV, the system exhibits PM (SSB) in the σ (τ) degrees of freedom and we have an (a) exponentially decaying (long-range) C_σ^x (C_τ^x).

To end this part, we notice that the exponential decay of the connected correlation $\tilde{C}_\tau^x(r)$ in Phase III and Phase IV means that the τ degrees of freedom are stabilized into a symmetry-breaking state instead of a GHZ state. The τ degrees of freedom do not evolve to a GHZ state due to the specific choice of the initial state in our work.

D. Effect of the single-site measurement τ_{2i-1}^x on the \mathbb{Z}_4 symmetric circuit model

In this section, we investigate the effect of the single-site operator τ_{2i-1}^x on the \mathbb{Z}_4 symmetric circuit model studied in the main text. Specifically, we set the occurring probability of the τ_{2i-1}^x measurement same as σ_{2i}^x and the probabilities satisfy $3p_t + p_\delta + 2p_h = 1$. As mentioned in the main text, the single-site measurement τ_{2i-1}^x is a relevant perturbation at the fixed point with two copies of percolation (e.g., the point $p_h = p_\delta = 0$) [49]. Therefore, the inclusion of the τ_{2i-1}^x measurement results in the disappearance of a stable gSPT region, leading to a different steady-state phase diagram, as shown in Fig. S9(a). This is in stark contrast to its equilibrium counterpart where $h \sum_i \tau_{2i-1}^x$ is an irrelevant perturbation, as depicted in Fig. S9(b). Since the line $p_h = 0$ has been investigated in the phase diagram shown in Fig. 3(a) in the main text, here, we focus on the case of $p_h > 0$ and study the two non-topological area-law phases therein.

For simplicity, we first consider the line $p_\delta = 0$. As displayed in Fig. S10(b1), the half-chain entanglement entropy

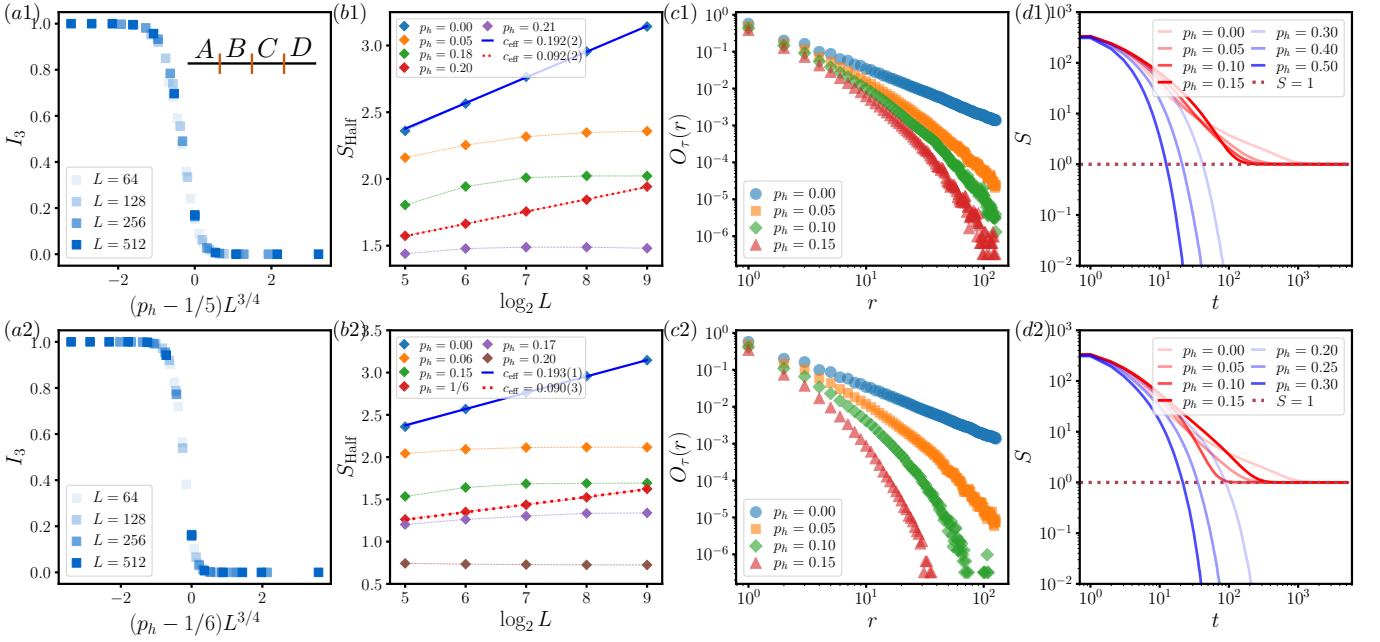


FIG. S10. The simulation results for the \mathbb{Z}_4 symmetric circuit model including the single-site perturbation τ_{2i-1}^x respectively in the case of $p_\delta = 0$ [(a1)-(d1)] and $p_h = p_\delta$ crossing the special point $p_h = p_\delta = 1/6$ [(a2)-(d2)]. (a1-a2) The data collapse of the generalized topological entanglement entropy S_{topo} . (b1-b2) The finite-size scaling of the half-chain entanglement entropy S_{Half} shows logarithmic growth at the percolation critical points. The blue solid and red dotted lines are least-squares fittings. (c1-c2) The string order parameter $O_\tau(r)$ as a function of the site distance r . (d1-d2) The purification dynamics of the full system entropy $S(t)$ versus the evolution time t . The simulated system size is $L = 256$ for (c1-c2) and $L = 512$ for (d1-d2) under open boundary conditions.

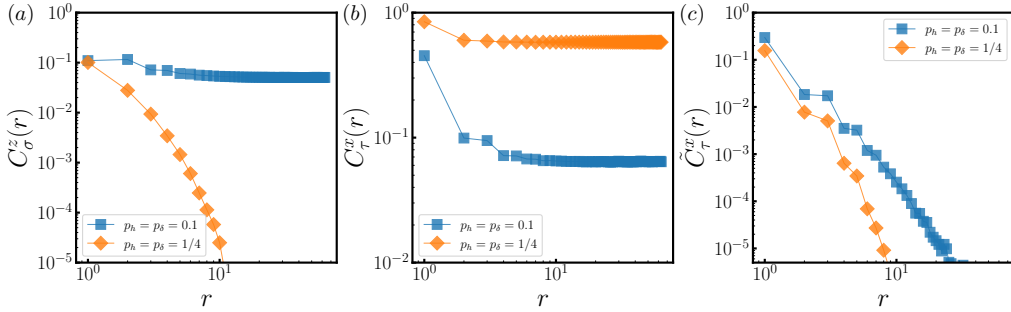


FIG. S11. Spin-spin correlations (a) $C_\sigma^z(r)$ and (b) $C_\tau^x(r)$ versus the site distance r for two representative points in the steady-state phase diagram shown in Fig. S9(a). (c) The connected correlation $\tilde{C}_\tau^x(r)$ for the same parameters. Simulations are performed with a system of size $L = 128$ under open boundary conditions.

S_{Half} grows logarithmically with the system size L at $p_h = 0$ ($p_h = 1/5$) characterized by an effective central charge $c_{\text{eff}} = 0.192(2)$ [$c_{\text{eff}} = 0.092(2)$] while S_{Half} saturates to a constant when L is large at other p_h values. This suggests a percolation transition between two area-law phases near $p_h = 1/5$. To determine the critical point, we employ the tripartite mutual information I_3

$$I_3 = S_A + S_B + S_C - S_{AB} - S_{BC} - S_{AC} + S_{ABC}, \quad (\text{S11})$$

where the whole system is equally partitioned into another four subsystems, $A|B|C|D$ [see Fig. S10(a1)]. In Fig. S10(a1), we calculate I_3 for various L as a function of p_h . The perfect data collapse of I_3 using $\nu = 4/3$ further confirms the percolation transition at the critical point $p_h = 1/5$. Interestingly, as illustrated in Fig. S10(c1), a small occurring probability p_h causes the string operator $O_\tau(r)$ changes immediately from algebraic to exponential decay implying that the single-site perturbation τ_{2i-1}^x gaps out the τ degrees of freedom and leads to an area-law phase. Furthermore, the residue entanglement entropy in the purification dynamics retains $S(t) = 1$ at late time for

$p_h < 1/5$. It can be explained by the \mathbb{Z}_2 SSB in σ degrees of freedom [note that $C_\sigma^z(r) \sim \text{const}$ at $p_h = p_\delta = 0.1$, see Fig. S11]. When $p_h > 1/5$, the symmetry breaking in σ degrees of freedom is restored [note that $C_\sigma^z(r)$ decays exponentially at $p_h = p_\delta = 0.4$, see Fig. S11] and the corresponding phase is trivially gapped both in τ and σ degrees of freedom as evidenced by a vanishing residue entropy $S(t \gg L) = 0$ [see blue lines in Fig. S10(d1)].

At last, the same simulations are performed for the case of $p_h = p_\delta$ and similar observations are made in Fig. S10(a2-d2). We also notice that the percolation line $5p_h + p_\delta = 1$ can be obtained by setting $p_h = p_t$ as the transition is just the SSB-PM transition happened in the σ chain.